Tracking the infiltration of molten salt into graphite using time-lapse X-ray micro-computed tomography

Xun Zhang [a,*], Alex Theodosiou [a,*], William Bodel [a], Phil Quayle [b], Ciara Fox [b], Chris Hankinson [b], Chris Morgans [b], Abbie N. Jones [a]

[a] *The Nuclear Graphite Research Group (NGRG), Department of Engineering for Sustainability, Henry Royce Institute, The University of Manchester, Oxford Road, Manchester, M13 9PL, UK*
[b] *MoltexFLEX, Rutherford House, Warrington Road, Birchwood, WA3 6ZH, UK*

ARTICLE INFO

ABSTRACT

For the first time, X-ray Micro-Computed Tomography (μ-CT) has been used to track the infiltration of molten salt into a porous graphite sample. Quantitative analysis on the X-ray μ-CT virtual slices enabled the extent of the salt infiltration and its spatial distribution within the graphite to be determined. The evolution of the pore structure is elucidated by direct comparison of the XCT micrographs before and after salt infiltration.

Molten Salt Reactors (MSRs) are a class of low-pressure, high-temperature nuclear fission prototype reactors for next generation advanced modular reactors that employ molten salt mixtures as the primary coolant and/or fuel. For thermal spectrum MSRs, graphite is typically utilised as moderator, reflector, and part of the core support structures [1]. The inherent porosity within the graphite means that it is prone to infiltration by the molten salt, resulting in changes in its properties. Such property changes must be taken into consideration during reactor design and a good understanding of interaction between molten salt and the graphite microstructure is therefore important in selecting graphite grades for applications in MSRs.

The graphite/molten salt interaction has traditionally been investigated using the weight gain after salt infiltration [2], followed by mercury intrusion porosimetry and post-mortem microstructure characterisations using, for example, Scanning Electron Microscopy (SEM). The results provided an overall description to the infiltration of molten salt into the graphite porosity. However, a more fundamental understanding of the graphite/molten salt interaction is still needed. How the pore size, shape, connectivity, and location with respect to the molten salt affect the detailed salt infiltration process remains to be understood.

As a non-destructive 3D microstructure characterisation technique, X-ray μ-CT can potentially deliver more detailed information for understanding the graphite/molten salt interaction. X-ray μ-CT has already been widely used for nuclear graphite studies elsewhere, focusing mainly on comprehensive microstructure characterisation. For example, the pore shape, size distribution, and type (open vs closed) within a range of nuclear graphite grades has been systematically characterised using X-ray μ-CT [3]. In addition, X-ray μ-CT has previously been combined with electron microscopy for multi-scale porosity analysis [4]. David Arregui-Mena et al. recently employed XCT to investigate the cracks generated by the infiltration of carbon forms into the CGB graphite used in the Molten Salt Reactor Experiment reactor [5]. Being non-destructive, X-ray μ-CT also enables the microstructure evolution at the same sample location to be investigated without inflicting damage to the sample. The resultant time-lapse micrographs enable the microstructure evolution to be traced back to its initial state. For example, Mostafavi et al. conducted a series of in-situ mechanical tests on nuclear graphite coupled with X-ray μ-CT and quantified crack opening behaviour by correlating the virtual volumes [6–8]. Since then, Liu et al. performed in situ mechanical testing coupled with real-time X-ray μ-CT at temperatures up to 1000 °C on Gilsocarbon nuclear graphite [9]. More recently, Wade-Zhu et al. recorded and compared crack propagation in virgin and neutron irradiated and radiolytically oxidised Gilsocarbon graphite using synchrotron X-ray μ-CT. The influence of neutron irradiation on the microstructure and cracking behaviour of the graphite was highlighted by following the fracture processes [10]. Bodel et al. also observed crack behaviour in bromine-intercalated graphite using in situ X-ray μ-CT to understand keyway root crack behaviour in reactor graphite bricks [11].
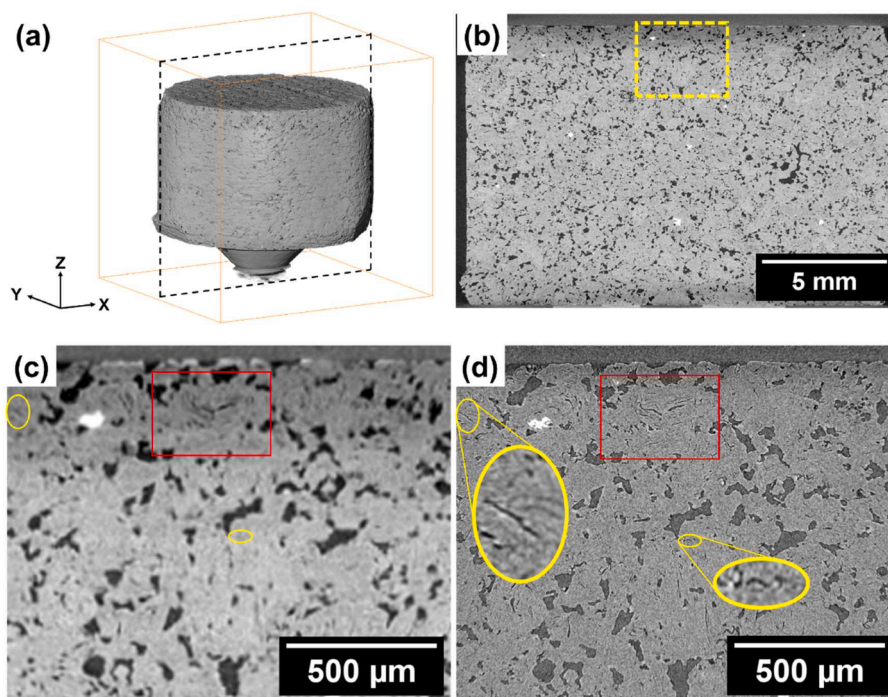

Fig. 1. XCT results of the virgin graphite (a) 3D volume rendering of the entire sample prior to salt infiltration from the global scan; (b) virtual slice through the middle of the sample as indicated by the black dash square in (a); (c) zoom-in view of the region in yellow box in (b) and (d) virtual slice from the high-resolution RoI scan of the same sample location as in (c). The yellow ellipses in (c) and (d) highlight some of the fine cracks that are invisible in the global scan. The red box shows an example of cluster of cracks that are visible in the global scans but are too fine to be confidently segmented for quantifying the porosity.

While time-lapse X-ray μ-CT has been extensively used for investigating the fracture behaviour of graphite, it can be equally insightful for use in studying molten salt impregnated samples and the detailed molten salt/graphite interaction; however, little such studies have yet been reported in the open literature. Previous work by Zhang et al. has used time-lapse X-ray μ-CT to track the infiltration of molten sand into a porous ceramic coating used for thermal insulation for gas turbine blades [12]. The detailed infiltration scenario and the consequences of the molten sand infiltration on the coating's microstructure have been revealed by comparing the micrographs at different stages of infiltration. More recently, Moon et al. used neutron CT to investigate a range of graphite grades subjected to FLiNaK salt infiltration at 750 °C and 5 bar pressure for 12 h [13]. For the first time, a direct visualization of the FLiNaK salt distribution within graphite has been achieved. However, the spatial resolution of neutron CT was low (~75 μm) and could not capture the detailed pore structures nor the individual salt phase inside the graphite pore network. In this work, X-ray μ-CT is used to investigate the detailed molten salt/graphite interaction by examining and comparing the micrographs recorded before and after salt infiltration at improved resolution. The aims are to explore the response of the graphite microstructure to molten salt impregnation, and to understand the role of graphite microstructure to its resistance to molten salt infiltration. This information will provide useful microstructural insights into the selection of graphite to be used in MSRs.

A medium-fine grain graphite has been used in this work. This is a synthetic graphite with an average nominal grain size of 800 μm [3]. For X-ray μ-CT, a cylinder with a radius of 8.5 mm and a height of 11 mm was cut out of the graphite block. The difficulty in preparing salt-impregnated samples on small specimens, combined with a desire to investigate salt infiltration over a large volume of material was the motivation for using samples larger than would otherwise be used with this technique. The sample was scanned using a Zeiss Xradia Versa 520 X-ray microscope (XRM) before and after molten salt infiltration. For each state, a low-resolution global scan and a high-resolution region-of-interest (RoI) scan were run. For all scans, the X-ray tube operated at

80 kV. The global scan covers the whole sample in the field of view and has a voxel size of 9.6 μm while the RoI scan was taken in the middle of the top surface with a voxel size of 1.9 μm.

The graphite sample was exposed to molten salt and corrosion control dopants by MoltexFLEX at their nuclear R&D laboratory in Warrington, UK. Samples were immersed in the salt environment at 795 °C within bespoke sealed steel chambers at a nominal pressure of 5 bar for 30 days.

Fig. 1 shows the XCT results taken before the graphite was infiltrated by the molten salt. The whole sample has been covered in the global scan as demonstrated in the 3D volume rending of the sample in Fig. 1(a) and the virtual slice through the middle of the cylinder in Fig. 1(b). A side-by-side comparison of the virtual slices from the global scan and high-resolution RoI scan in Fig. 1(c and d) show examples of fine cracks (yellow ellipse) that are too small to be resolved in the global scan in Fig. 1(c). For planar defects such as cracks, they can be detected in X-ray μ-CT even if they are smaller than the voxel size [14] (e.g. those in the red square in Fig. 1). However, they are too small in one dimension to be confidently segmented and quantified.

The X-ray tomographs taken before and after salt infiltration were aligned and registered so that the microstructure at the same sample locations can be compared. Virtual slices from the global scans through the middle of the cylinder's axis and virtual slices from the high-resolution RoI scans ~1 mm below the sample surface are compared in Fig. 2. The bright phases in the virgin sample in Fig. 2(a) and (c) correspond to impurities, typically Ni and Fe [15], a result of their higher X-ray attenuation coefficients than carbon.

Fig. 2(b) shows that after molten salt infiltration, many pores have become filled by the salt. The salt appears brighter than the graphite but darker than the impurities. While the salt has reached the centre of the sample, not all pores have been filled. In fact, some pores that are relatively close to the cylinder's lateral surface remain unfilled (e.g. those indicated by the yellow arrows in Fig. 2(b)). Moreover, some pores appear to have been partially filled. This could be a result of the larger thermal contraction of the salt as the salt and graphite cooled from the
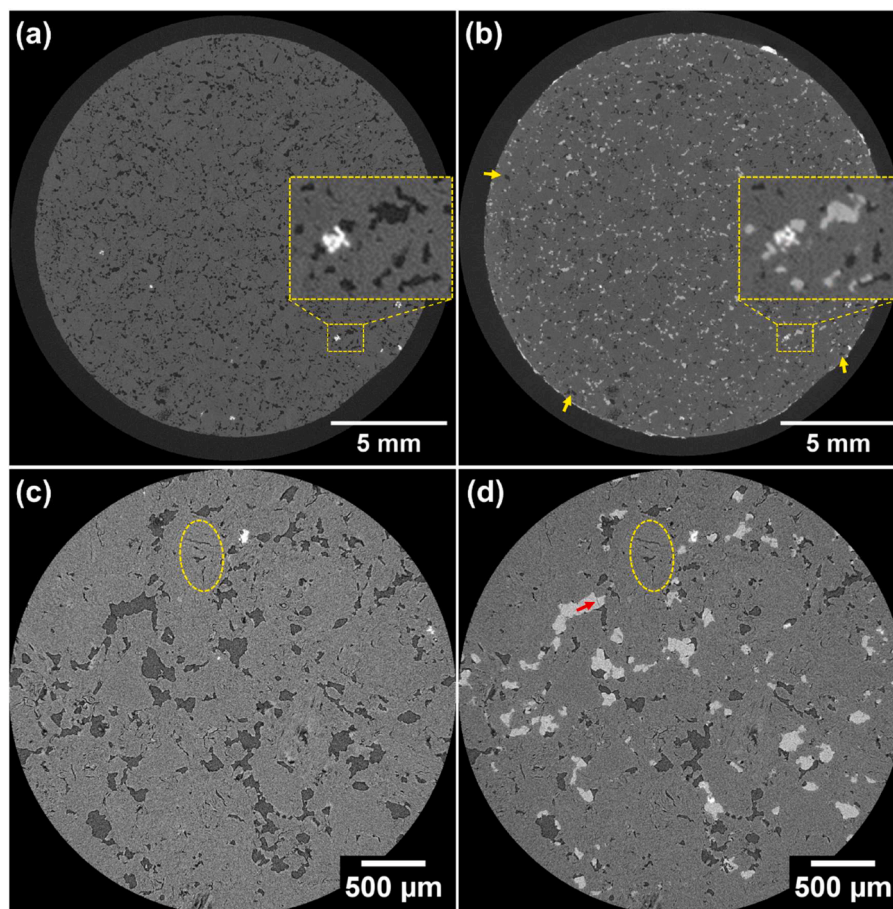
Fig. 2. X-ray μ-CT virtual slices from the global scans through the middle of the cylinder: (a) before and (b) after molten salt infiltration for 30 days. The bright phase in (a) corresponds to metallic impurities. The salt in (b) is brighter than the graphite but darker than the impurities. (c) and (d) virtual slices from the RoI scans ~1 mm below the sample surface before and after salt infiltration. The yellow ellipses highlight cracks that are not filled by the salt. The red arrow indicates a crack in the salt.
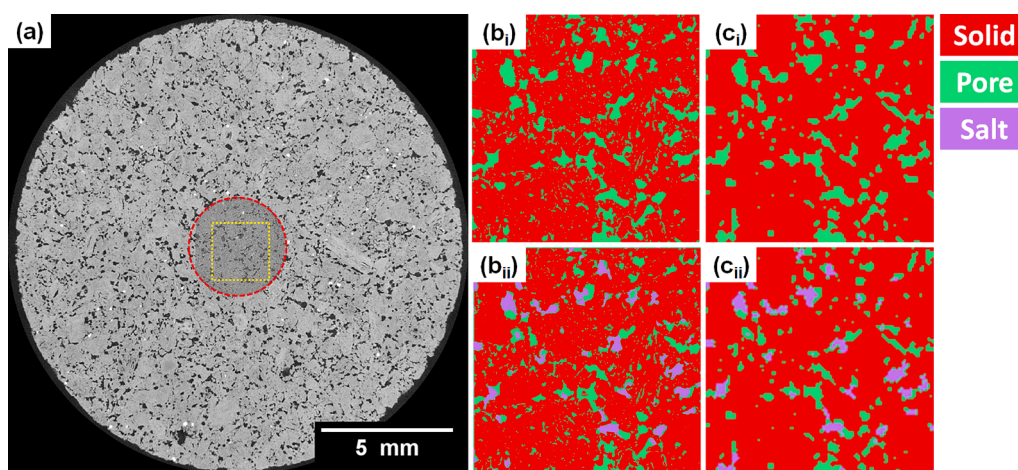

Fig. 3. (a) Virtual slices showing the virgin graphtie sample from the global scan superimposed by the RoI scan (red circle). The yellow square highlightd the region for segmentation; (b) segmented images from the RoI scans and (c) segmented images from the global scans before and after salt infiltration.

infiltration temperature to room temperature. Zoom-in view from the high-resolution RoI scans (Fig. 2(d)) show that the salt has mainly filled the larger pores. The cracks and fine pores have remained salt-free. The pores are not fully filled by the salt and gaps exist between the salt and the graphite. Cracks are also found within the salt.

In order to quantify the porosity and the fraction of those that have

been filled by the salt, the virtual slices have been segmented using the Trainable Weka Segmentation plugin in Fiji [16]. This is a machine learning tool to classify the voxels in the X-ray μ-CT virtual volume into groups representing the graphite, the pores, and the salt respectively. Features of the input images are constructed using a range of image filters. A classifier is created and trained from manually selected voxels

Table 1
Volume fraction of the phases determined from segmented XCT tomographs.

	Virgin sample		Infiltrated sample		
	Pore	Graphite	Residual Pore	Salt	Graphite
Volume fraction (%)	16.2 ± 0.41	83.8 ± 0.41	10.7 ± 0.27	5.5 ± 0.31	83.8 ± 0.44

for each phases according to their representations of the features of the images. Once trained, the classifier is applied to the whole stack of the virtual slices. From the segmented images, the volume fraction of the pores and the salt can be computed directly by counting the number of voxels for each phase.

Ideally, virtual slices from the high-resolution scans should be used for quantitative analysis. However, more than 100 such scans need to be stitched to cover the whole sample. Collecting the XCT virtual slices and quantifying them is practically impossible. Therefore, the global scans are used for the quantitative analysis of the salt. To estimate the influence of the compromised resolution of the global scan on the quantification, results from a slice taken at roughly the same sample location from the global and RoI scans are compared. The slices used for this analysis are shown in Fig. 3. For this specific region, the volume percentage of the pore in the virgin graphite and salt (after infiltration) are 16.1 % and 5.8 %. Those from the RoI scans are 19.8 % and 5.1 % respectively.

While the porosity determined from the RoI scan is more than 3 % higher than that from the global scan, both results are lower than the value (i.e. ~21 %) derived using the theoretical density (2.27 g/cm^3) and the nominal density (1.79 g/cm^3) for the graphite [15]. The difference is smaller for the high-resolution RoI scan as the finer cracks can be resolved and contribute to the total volume of pores.

It is worth emphasising that in the present work, we are not trying to accurately determine the porosity. Instead, we are aiming at observing the microstructure change due to the salt infiltration. Therefore, it is the changes in the tomographs taken before and after molten salt infiltration that are of interest. In this respect, the global scan and RoI scan have yielded comparable results i.e. the salt volume fractions are comparable. This is a result of the fact that the fine cracks have remained salt-free after infiltration (see Fig. 2(d)). This observation also corroborates the use of the global scan for quantitative analysis of the salt regardless of its relatively low spatial resolution.

Table 1 compares the average volume fractions of the pores and infiltrated salt, based on the segmented global tomographs. It is worth mentioning that the image quality was degraded towards the top and bottom of the sample due to the cone beam geometry of the X-ray μ-CT

scanner. Therefore, the image stack was cropped by ~1.7 mm from the top and bottom to generate the results in Table 1.

According to Table 1, approximately 34 % of the pores that have been resolved in the global scan become filled with the salt after infiltration at 795°C under 5 bar for 30 days. This fraction could be higher at the infiltration temperature since the coefficient of thermal expansion of the salt is around one order of magnitude higher than that of the graphite and the salt has shrunk more than the graphite upon cooling from the infiltration temperature.

The spatial distribution of the infiltrated salt is of interest as it contains more details about the infiltration kinetics. In order to directly visualise the spatial distribution of the salt, a local coordinate is defined with its origin located at the centre of the bottom surface of the cylindrical sample. The cylinder is divided into 10 equal-volume sub-regions
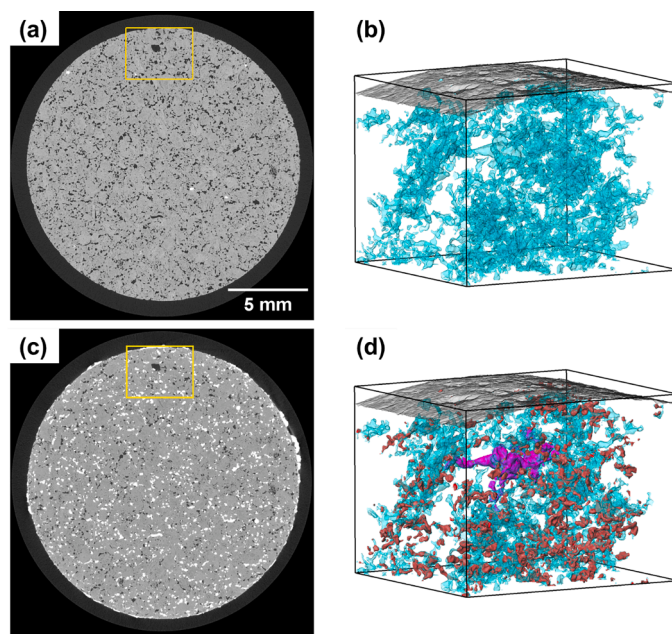

Fig. 5. Pore structure before and after infiltration. (a) and (c) virtual slices showing a region with relatively lower salt volume fraction guided by Fig. 3. The yellow boxes contain the pore of interest and are analysed in 3D. (b) 3D surface view of the pore network to which the pore of interest belonged before salt infiltration. The sample side surface is also highlighted in grey. (d) 3D surface view of the pore of interest in purple after infiltration and the salts in red. The residual pores are also included.
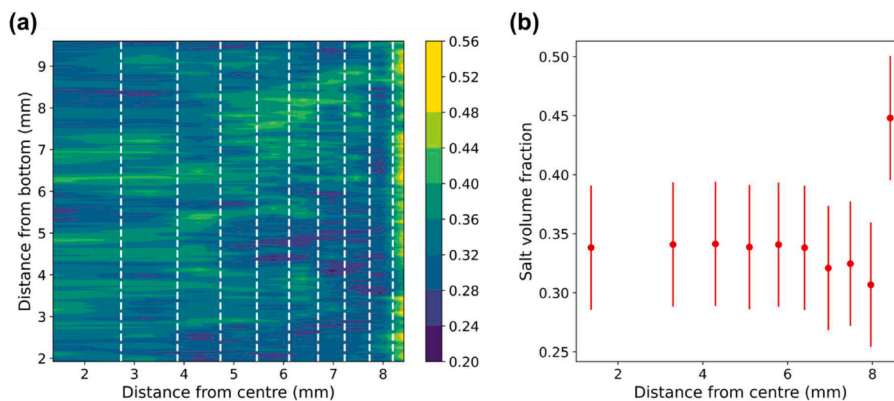

Fig. 4. Spatial distribution of the infiltrated salt. (a) Volume fraction of the infiltrated salt over the pores (filled ones and residual empty ones) as functions of the distance from the centre and bottom of the cylinder. The white dash lines highlight the boundaries of the sub-regions. For the annular cylinders, the locations of their middle planes between their outer and inner surfaces are used as the distance from centre. (b) Averaged over the height of the cylinder. The error bars represent the standard variations along the height direction. Note that the cylinder was cropped by ~1.7 mm from the top and bottom.
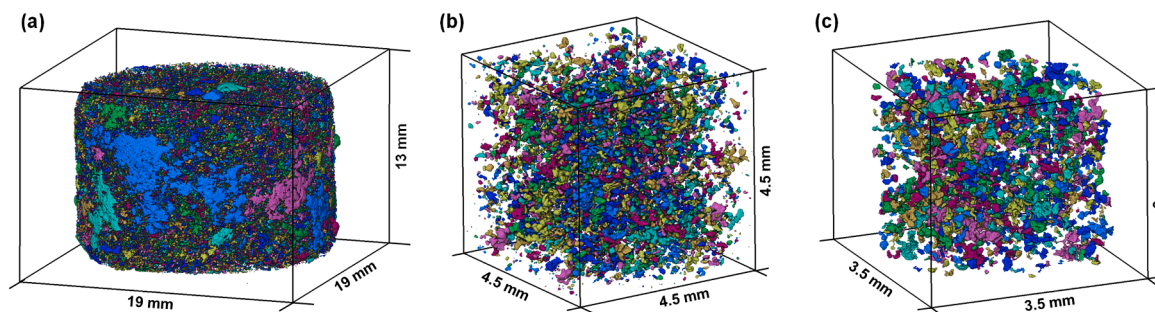
Fig. 6. 3D volume rendering of the salt. Each colour represents a spatially connected salt cluster: (a) whole sample from the global scan. Large patches of the salt are found on the sample surface; (b) a sub-volume inside the sample from the global scan and (c) a sub-volume inside the sample from the RoI scan.

(1 solid cylinder and 9 annular cylinders) and the volume ratio of the infiltrated salt over the pore is computed in each sub-region from the segmented tomographs. The computed volume fraction distribution of the infiltrated salt is plotted in Fig. 4(a) which is further averaged along the height and plotted in Fig. 4(b). Fig. 4 shows that except for the regions near the side of the cylinder, the salt infiltration is generally uniform. While regions of relatively high (e.g. 6.5 mm from the centre and 8 mm from the bottom) and low (e.g. 7 mm from the centre and 4 mm from the bottom) salt fractions can be observed, there is no clearly defined trend in the salt volume fraction towards neither the top/bottom nor the centre of the cylinder. It is apparent though that the outermost annular cylinder has the most infiltrated salt, due to its direct contact with the salt.

Guided by Fig. 4(a), it is possible to navigate to regions where the volume fraction of the infiltrated salt is relatively low (e.g. the dark blue region about 7 mm from the centre and 4 mm from the bottom). The characters of the pores at such regions can be investigated further in 3D to explore why they have been more resistant to the infiltrating salt.

Fig. 5 shows details of a large pore before and after the infiltration process, which appears unfilled post-infiltration. Using the "magic wand" tool in Avizo Software (a region growing segmentation tool) on the virtual slices for the virgin sample, the pores that are initially connected to the pore of interest can be segmented. Fig. 5(b) shows the 3D surface view for the pores that are connected to the pore of interest in space within the RoI. As can be seen, the pore of interest is in fact connected to a complicated pore network which reached the sample side surface (i.e. it is an open pore).

Fig. 5(d) highlights the pore of interest after salt infiltration in purple together with the salt, highlighted in red. The unfilled pore is close to the surface, but it is more spherical. It is unlikely that the pore has become unfilled during cooldown given its geometry and size; the authors postulate that gas might have been trapped inside the pore during infiltration, preventing the pore from being filled. Infiltration under vacuum conditions can be employed together with the time-lapse X-ray μ-CT to confirm this hypothesis in future work. Notice that after salt infiltration, the connectivity of the pore network is broken by the salt and the pore of interest has become isolated.

The salt was analysed further by applying a connected components labelling in 3D to the binarized images where only the salt phase has been highlighted. Fig. 6 shows the salt clusters in 3D. Each cluster is rendered in one colour. As can be seen in Fig. 6(a), large salt clusters only exist on the sample surface. Inside the sample, the salts are isolated. The high-resolution RoI scan yields the same results as shown in Fig. 6 (c). It is expected that at the infiltration temperature, the salt was liquid and should have been in one piece. The fact that it is scattered as isolated small clusters inside the sample at room temperature could be a result of shrinkage as the sample cooled down given that the coefficient of thermal expansion of the salt is much higher than that of the graphite.

In summary, this work successfully demonstrated for the first time the use of time-lapse X-ray μ-CT in tracking molten salt infiltration into a graphite sample. Being non-destructive, the time-lapse μ-CT provided a direct comparison of the graphite's microstructure before and after molten salt infiltration, enabling the relative volume of pores that have been filled by the salt to be quantified. Moreover, the time-lapse X-ray μ-CT scans covering the whole sample, validated by the local yet high-resolution RoI scans, have delivered detailed information about the spatial distribution of the infiltrated salt and the 3D structures of the infiltrated salt. All of this provides valuable information for the understanding of the kinetics that control the molten salt infiltration into the porous graphite.

The outcomes of this work also point to the following future work:

- More systematic study on the effects of infiltration conditions including temperature, salt compositions, gas pressure etc. and salt compositions using the methodology developed in this work;
- The XCT result on the virgin sample can be used to construct computational fluid mechanics (CFD) models to predict the salt infiltration while the results on the infiltrated sample can be readily used to validate the model results;
- Effect of pore filling on the mechanical properties employing finite element (FE) models derived directly from the X-ray μ-CT virtual volumes.

Declaration of competing interest

The authors declare that they have no known competing financial interests or personal relationships that could have appeared to influence the work reported in this paper.

Acknowledgements

References

[1] J.J. Lee, J.D. Arregui-Mena, C.I. Contescu, T.D. Burchell, Y. Katoh, S.K. Loyalka, Protection of graphite from salt and gas permeation in molten salt reactors, J. Nucl. Mater. 534 (2020).

[2] Z. He, L. Gao, W. Qi, B. Zhang, X. Wang, J. Song, X. He, C. Zhang, H. Tang, R. Holmes, H. Xia, X. Zhou, Molten FLiNaK salt infiltration into degassed nuclear graphite under inert gas pressure, Carbon. N. Y. 84 (2015) 511–518.

[3] J.D. Arregui-Mena, R.N. Worth, W. Bodel, B. März, W. Li, A.A. Campbell, E. Cakmak, N. Gallego, C. Contescu, P.D. Edmondson, Multiscale characterization and comparison of historical and modern nuclear graphite grades, Mater. Charact. 190 (2022).

[4] M. Jiang, A. El-Turke, G. Lolov, K. Ammigan, P. Hurh, D. Liu, Multiple length-scale microstructural characterisation of four grades of fine-grained graphite, J. Nucl. Mater. 550 (2021).

[5] J.D. Arregui-Mena, P.D. Edmondson, D. Cullen, S. Levine, C. Contescu, Y. Katoh, N. Gallego, Microstructural characterization of the CGB graphite grade from the molten salt reactor experiment, J. Nucl. Mater. 582 (2023).

[6] M. Mostafavi, S.A. McDonald, P.M. Mummery, T.J. Marrow, Observation and quantification of three-dimensional crack propagation in poly-granular graphite, Eng. Fract. Mech. 110 (2013) 410–420.

[7] M. Mostafavi, S.A. McDonald, H. Çetinel, P.M. Mummery, T.J. Marrow, Flexural strength and defect behaviour of polygranular graphite under different states of stress, Carbon. N. Y. 59 (2013) 325–336.

[8] M. Mostafavi, N. Baimpas, E. Tarleton, R.C. Atwood, S.A. McDonald, A. M. Korsunsky, T.J. Marrow, Three-dimensional crack observation, quantification and simulation in a quasi-brittle material, Acta Mater. 61 (16) (2013) 6276–6289.

[9] D. Liu, B. Gludovatz, H.S. Barnard, M. Kuball, R.O. Ritchie, Damage tolerance of nuclear graphite at elevated temperatures, Nat. Commun. 8 (1) (2017).

[10] J. Wade-Zhu, R. Krishna, A.J. Bodey, M. Davies, N.K. Bourne, C. Rau, B. Davies, A. Tzelepi, A.N. Jones, B.J. Marsden, P.M. Mummery, 4D synchrotron X-ray microtomography of fracture in nuclear graphite after neutron irradiation and radiolytic oxidation, Carbon. N. Y. 168 (2020) 230–244.

[11] W. Bodel, P. Martinuzzi, B. Davies, A. Steer, T. Lowe, P. Mummery, Mimicking irradiation-induced cracking of nuclear graphite using bromine intercalation, Scr. Mater. 199 (2021).

[12] X. Zhang, X. Shan, P.J. Withers, X. Zhao, P. Xiao, Tracking the calcium-magnesium-alumino-silicate (CMAS) infiltration into an air-plasma spray thermal barrier coating using X-ray imaging, Scr. Mater. 176 (2020) 94–98.

[13] J. Moon, N.C. Gallego, C.I. Contescu, J.R. Keiser, D. Sulejmanovic, Y. Zhang, E. Stringfellow, A neutron tomography study to visualize fluoride salt (FLiNaK) intrusion in nuclear-grade graphite, Carbon. N. Y. 213 (2023).

[14] E. Maire, P.J. Withers, Quantitative X-ray tomography, Int. Mater. Rev. 59 (1) (2013) 1–43.

[15] G.B. Engle. *Properties of unirradiated HTGR core support and permanent side reflector graphites: PGX, HLM, 2020, and H-440N.* United States, 1977. https://doi.org/10.2172/7096077.

[16] I. Arganda-Carreras, V. Kaynig, C. Rueden, K.W. Eliceiri, J. Schindelin, A. Cardona, H. Sebastian Seung, R. Murphy, Trainable Weka Segmentation: a machine learning tool for microscopy pixel classification, Bioinformatics. 33 (15) (2017) 2424–2426.